Acta Geodyn. Geomater., Vol. 9, No. 4 (168), 521–540, 2012

THE MATRIX POROSITY AND RELATED PROPERTIES OF A LEUCOCRATIC GRANITE FROM THE KRUDUM MASSIF, WEST BOHEMIA

Lucie NOVÁKOVÁ [1)]*, Karel SOSNA [2)], Milan BROŽ [1)], Jan NAJSER [2)] and Petr NOVÁK [3)]

[1)] *Institute of Rock Structure and Mechanics, Academy of Sciences of the Czech Republic, v.v.i., V Holešovičkách 41, 182 09 Prague, Czech Republic*
[2)] *ARCADIS Geotechnika Inc., Geologická 4, 152 00, Prague 5, Czech Republic*
[3)] *ISATech Ltd., Osadní 26, 170 00, Prague 7, Czech Republic*
**Corresponding author's e-mail:* lucie.novakova@irsm.cas.cz

(*Received* May 2012*, accepted* September 2012)

ABSTRACT
This paper investigates the matrix porosity and related properties of a leucocratic granite from the Krudum Massif, West Bohemia. The required samples were obtained from the 30-year old core of borehole KZ-25 (Material Documentation Depositories). In total, nine sample sets were taken from different depth levels within the borehole ranging from 18 m to 108 m. The hydraulic conductivity of the granite matrix was measured using a pressure cell whilst standard methods were employed to determine the dry density, connected porosity and total porosity. The pore size distribution was analysed using mercury porosimetry. The ultrasonic velocities were measured using a pulse source and oscilloscope. Dynamic Young's modulus, dynamic shear modulus, Poisson's ratio, static Young's modulus, uniaxial compressive strength and moisture were determined according to measurements of ultrasonic velocities and deformability in uniaxial compression. The morphology and structure of the pore network was studied using high resolution scanning electron microscopy. The overall porosity values defined by the different porosimetry methods follow the same trends although the absolute values differ according to the specific method. A logarithmic relationship was found to exist between hydraulic conductivity and porosity within the granite matrix. In addition, a slight depth dependence was noted in the porosity, hydraulic conductivity, bulk density, and ultrasonic velocities of the granite matrix. The SEM images have allowed precise mapping and detailed description of the pore network.

KEYWORDS: leucocratic granite; matrix porosity; geomechanical properties; hydraulic conductivity; ultrasonic velocities; scanning electron microscopy

1. INTRODUCTION

The nature and origin of granites has intrigued earth scientists for hundreds of years (Pitcher, 1997). In order to obtain detailed information about the characteristics of a specific granitic rock it is important to study its physical, geomechanical, and chemical properties. These properties may be greatly modified where the rock is fractured. These data, in addition to an understanding of the present geological setting of the granite, are essential when planning the construction of artificial underground structures such as tunnels, radioactive waste repositories, and storage facilities for oil or natural gas. Schild et al. (2001) studied a granite matrix using a range of petrophysical methods to determine its porosity, permeability, and P-wave velocity. Hamm et al. (2007) concluded that the hydraulic parameters of fractured rocks need to be assessed precisely in order to understand the relationship between the hydraulic conductivity and fracture properties.

A number of studies have shown that the ultrasonic pulse velocity test provides a useful and reliable non-destructive tool for assessing the structure of rock. The internal damage within a material may be seen from its mechanical characteristics as defined by the modulus of elasticity and compressive strength (Hassan et al., 1995) while structural irregularities may be detected by ultrasonic tests (Schild et al., 2001; Zinszner et al., 2002; Vasconcelos et al., 2008; Chaki et al., 2008; Nováková et al., 2011). The most popular and rapid method of pore structure analysis in a wide variety of porous materials is that of mercury porosimetry (Ritter and Drake, 1945). This technique enables the size and volume of mesopores and macropores to be measured in solid porous rocks. It is based on the property of mercury to behave as a non-wetting liquid in a variety of solid materials. The measurement of pore-size distribution is complicated by the fact that most porous materials are characterised by irregular pore shapes; this may be overcome if it is assumed that all pores have a common geometric shape (Felch and Shuck, 1971). A model for such pore surfaces was developed by Good and Mikhail (1981). In the model, pores are represented by cylinders. In reality, pore surfaces are very rough and contain void spaces that correspond to the entrance of branch pores.

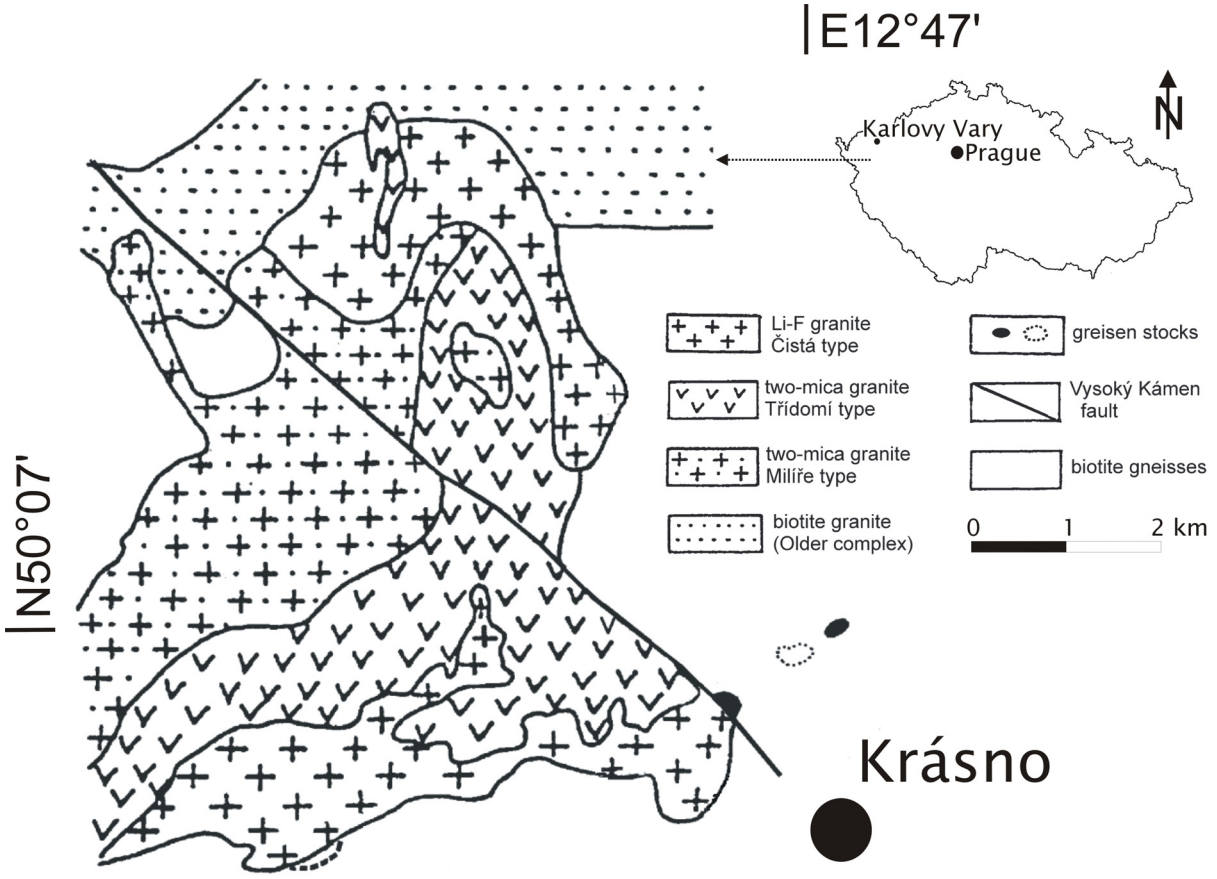

Fig. 1 A geological sketch of the Krudum Massif (modified after René, 1998).

Scanning Electron Microscopy (SEM) and stereological analysis form valuable tools with which to characterise microcracks in granites (Hommand-Etienne and Houpert, 1989). The use of a high-resolution microscope is comparatively inexpensive and may be undertaken on a considerable range of samples (Bogner et al., 2006). However, the imaging and analysis of single features (e.g. pores, cracks, microfissures) by electron microscopy is usually limited to very small areas (Helmuth et al., 1999). The strong relationship that exists between the rock microstructure and its physical properties was confirmed by David et al. (2000). Machek (2011) used SEM to determine cracks within granite rock and it was concluded that the majority of the granite matrix porosity could be attributed to grain-boundary and cleavage cracks. This microcracking depends upon the rock mineralogy, fabric, and microstructure (Akesson at al., 2004).

By combining various methods it is possible to accurately characterise the rock, especially its composition and microstructures. In this paper, the results of a number of laboratory methods applied to samples taken from a single core are described and compared. The presented data form a small part of the comprehensive research project, "Research of an influence of a granite matrix porosity over a radio-active waste geological disposal safety including methodology and measuring devices development". The main objectives of this paper are to outline a coherent approach to investigating granite matrix porosity, to compare the applied methods, and to consider the implications of recent studies of granite matrix.

2. GEOLOGICAL SETTING

The studied locality is situated near town Krásno, 20 km southwest of Karlovy Vary town in western Bohemia (Fig. 1). Borehole KZ-25 was drilled in 1974 during prospecting for a nearby feldspar quarry (Vysoký Kámen Quarry). The borehole was located in the eastern part of the Krudum Massif. This massif is a broadly triangular granite body covering 50 km^2. The central part of the massif comprises a porphyritic two-mica granite (the Třídomí Granite) while its western part is dominated by a two-mica granite (the Milíře Granite). The southern and eastern margins of the massif comprise the youngest and the most fractionated topaz-albite granite (the Čistá Granite) (Jarchovský, 2006). Post-magmatic brittle deformation has given rise to a suite of mineralogically distinct veins (barren quartz, quartz-cassiterite, quartz-wolframite, quartz-arseno-pyrite, quartz-fluorite, and quartz-hematite) (Dolníček

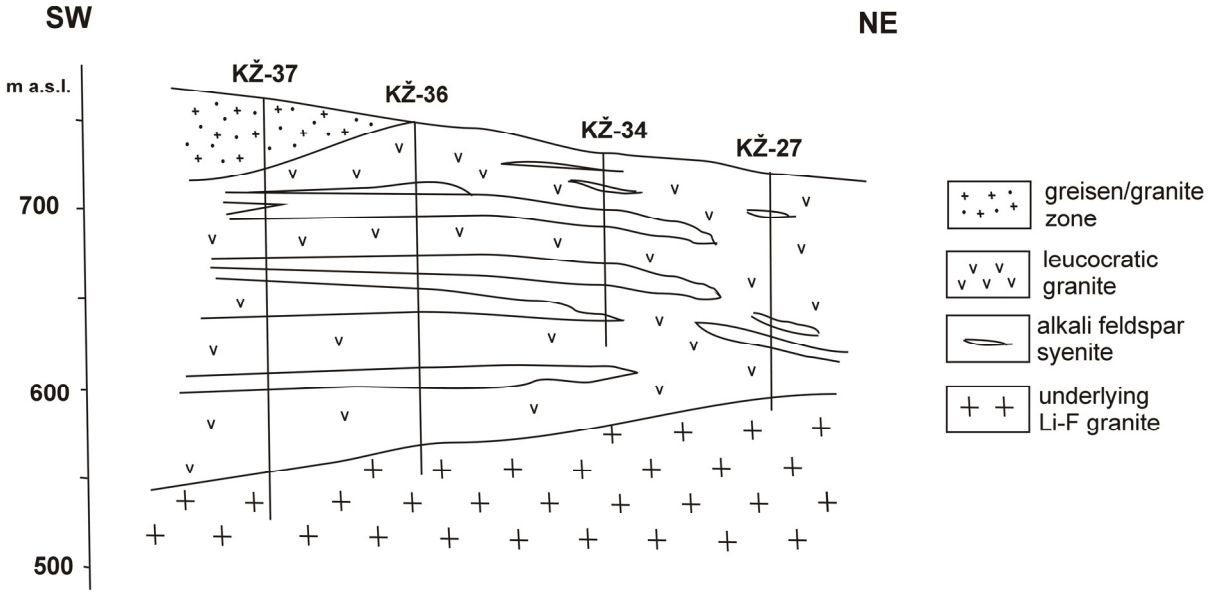

Fig. 2 A cross-section through the area around Vysoký Kámen (modified after Jarchovský, 2006). The KZ-25 borehole was drilled about 90 m to the northwest of this profile.

Table 1 Description of the rocks within borehole KZ-25 (Pácal and Pavlů, 1979).

Depth [m]	Rock
0.0 – 1.5	Clay
1.5 – 7.0	Eluvium of the leucogranite
7.0 – 16.85	Weathered leucogranite
16.85 – 22.7	Alkali feldspar syenite
22.7 – 26.3	Alkali feldspar syenite with quartz
26.3 – 31.8	Leucogranite
31.8 – 32.8	Alkali feldspar syenite
32.8 – 37.5	Leucogranite
37.5 – 38.5	Alkali feldspar syenite
38.5 – 43.7	Leucogranite
43.7 – 44.7	Pegmatite
44.7 – 94.7	Leucogranite
94.7 – 95.15	Alkali feldspar syenite
95.15 – 100.4	Leucogranite
100.4 – 101.7	Alkali feldspar syenite
101.7 – 106.6	Leucogranite
106.6 – 107.4	Alkali feldspar syenite
107.4 – 119.5	Leucogranite
119.5 – 123.0	Granite with micas
123.0 – 126.0	Aplite
126.0 – 205.0	Li-topaz granite

et al., 2012). The southeastern margin of the Krudum Massif is cut by the ENE-WSW trending Vysoký Kámen Fault. The western block uplifted along this fault and was then eroded (Jarchovský, 2006).

The KZ-25 borehole was drilled in an area of leucocratic granite with alkali feldspar syenite layers lying on the basal Li-F granite (Jarchovský, 2006; Fig. 2). The leucocratic granite is medium to fine grained. In this granite, micas are rare and the Na-feldspar to K-feldspar ratio varies significantly (from 0.5 to 2.5). The granite is locally composed by alkali feldspar syenite, a rock with no micas and a low quartz content (Streckeisen, 1974) (Table 1, Table 2). Numerous small pegmatite bodies of veins of irregular shape and smudge-like pegmatite bodies were also found in the quarry (Rukavičková et. al, 2009). The location of the borehole has now been quarried for raw feldspar.

3. EXPERIMENTAL PROCEDURE

3.1. SAMPLING AND CHEMICAL ANALYSIS

The KZ-25 core is stored in the Material Documentation Depositories of the Czech Geological Survey. The required samples were taken from this core at depth levels of 18, 28, 38, 48, 58, 76, 88, 98, and 108 metres (Fig. 3), Figure 4 shows the polished samples prepared from these samples. The diameter of the original core is 150 mm while that required for most tests is 50 mm. Therefore, a new core with the required diameter was cut from the original. Samples with heights of 10, 20, 50, and 100 mm were then cut from the new core using a water-cooled diamante saw. In this paper, these samples are referred to as 'unsaturated'. A macroscopic petrological description of the samples was then conducted. To determine the chemical composition of the rocks within the KZ-25 borehole, chemical analyses of rocks were undertaken in the laboratory of Czech Geological Survey.

3.2. CONNECTED AND TOTAL POROSITY

The required samples (h = 50 mm; d = 50 mm) were cut from the original core and then oven dried for 24 hours at 105 °C. During heating and cooling,

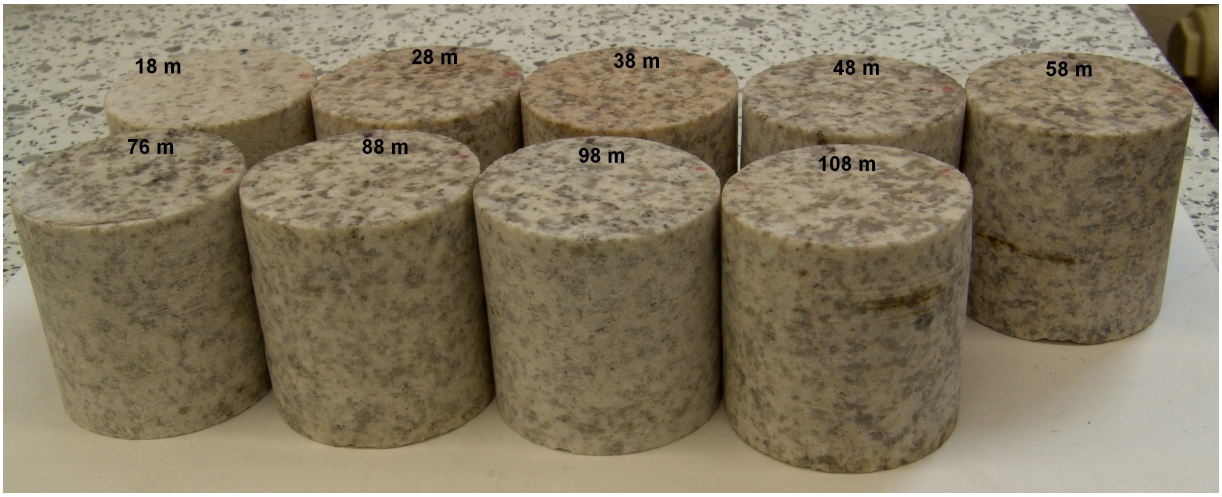

Fig. 3 The studied samples from KZ-25 borehole.

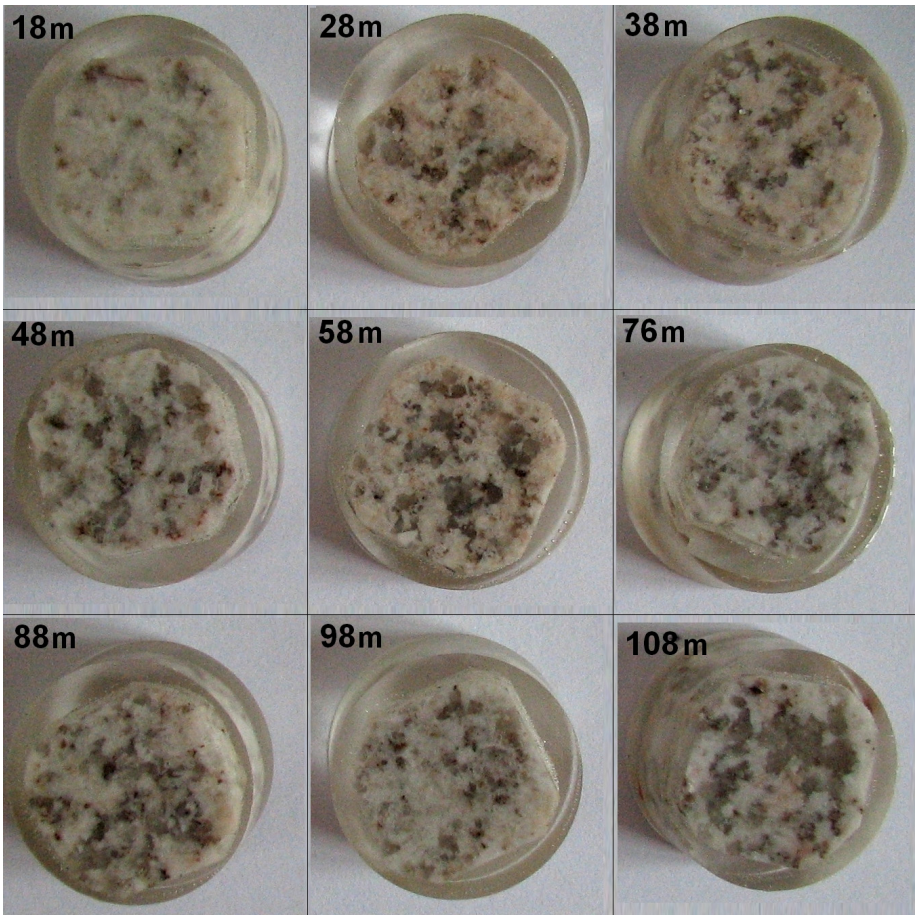

Fig. 4 Photographs of the polished samples prepared for SEM.

the temperature was changed gradually by 0.3 °C/min so as to prevent any cracking that may result from the development of a high temperature gradient inside the sample (Reuschlé et al., 2006; Chaki et al., 2008). Following temperature equalisation, the specimens were water saturated under vacuum as proposed by ISRM (1977). The specimens were kept under vacuum for 24 hours before being submerged by water at atmospheric pressure for between 24 hours to several days to allow the saturation. The connected porosity (n_{ISRM}) was obtained by weighing the saturated m_{sat} and dry m_d samples, respectively (Eq. 1),

$$n_{ISRM} = \frac{m_{sat} - m_d}{m_{sat} - m_{sat}'} \quad (1)$$

where m_{sat}' is the weight of the saturated sample immersed in water. An alternative calculation of the connected porosity (n_{hc}) was also undertaken to assess the influence of the measuring procedure: the value of m_{sat} measured after the hydraulic conductivity test was used in Eq. 1. The total porosity (n_T), which includes isolated voids and microfractures, was calculated from Eq. 2,

$$n_T = 1 - \frac{\rho_d}{G_s} \quad (2)$$

where specific gravity G_s was determined through a standard test procedure in a pycnometer and dry density ρ_d was calculated as a ratio of m_d and volume V. The moisture (W) was calculated using Eq. 3, where m_{sat} is saturated and m_d dry sample, respectively.

$$W = \frac{m_{sat} - m_d}{m_d} \quad (3)$$

3.3. MERCURY (HG) POROSIMETRY

The Pascal 140+240 (Thermo Scientific) mercury injection system was used to determine the connected porosity of the samples. Porosity and open pore size distribution of each sample were computed using the PASCAL (Pressurization with Automatic Speed-up by Continuous Adjustment Logic) method and the Washburn (1921) equation (Eq. 4):

$$pr = -2\,\mu\cos\Theta \quad (4)$$

where p is pressure, r pore radius, μ surface tension, and Θ contact angle.

The apparatus uses pressure interval from 0.1 kPa to 200 MPa and from this it is possible to identify pores with widths ranging from 3.7 nm to 58 μm. The pressure applied depends on the size of the threshold controlling access to the void. The measurement of the injected mercury volume at different steps of increasing pressure gives the volume of pores for a range of thresholds.

3.4. HYDRAULIC CONDUCTIVITY

The saturated samples (h = 50 mm; d = 50 mm) were placed in the pressure cell. Figure 5 shows a sketch of a sample during the test. Both upper and lower surfaces were connected to pressure controllers manufactured by GDS Ltd. The cell pressure was kept constant during all tests, at σ_c = 1000 kPa. The average effective stress inside the specimens corresponded to the average effective stress of the specimens in particular depths *in situ*. A constant pressure difference between upper and lower surfaces of Δ = 50 kPa was kept during the test and the volume of water that passed through the sample was recorded.

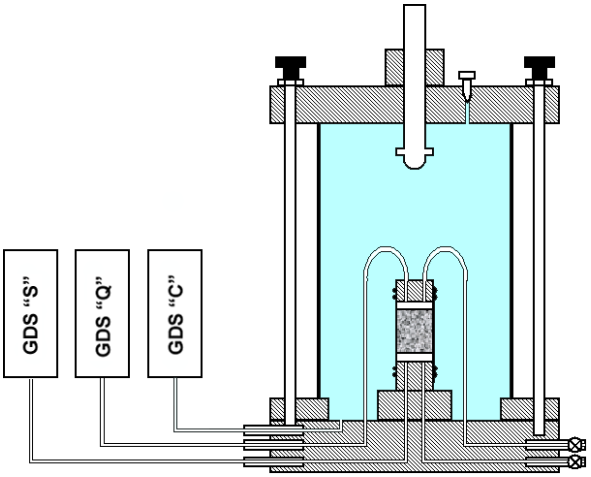

Fig. 5 A sketch of the pressure cell and controllers used for the measurement of hydraulic conductivity.

3.5. ULTRASONIC VELOCITIES

P-wave and S-wave velocities were measured vertically in the samples (h = 50 mm; d = 50 mm) using an apparatus that comprised two pairs of piezosensors, a precise impulse generator, and an oscilloscope. The two pairs of piezosensors, V103 and V153 (Olympus), were used as transmitter and receiver respectively. The resonance frequency of the sensors was 1 MHz. The contact between the sensors and sample was improved using ultrasonic couplant. The saturated and oven dried samples were measured in accordance with that proposed by ISRM (1978). Length to diameter ratio of 1 was used due to feasibility of hydraulic conductivity measurement. Dynamic Young's modulus E_d (Eq. 5), dynamic shear modulus G_d (Eq. 6), and Poisson's ratio ν (Eq. 7) were calculated according to (Zisman, 1933).

$$E_d = \frac{\rho v_S^2 \left(3v_P^2 - 4v_S^2\right)}{v_P^2 - v_S^2} \quad (5)$$

$$G_d = \rho v_S^2 \quad (6)$$

$$\nu = \frac{v_P^2 - 2v_S^2}{2\left(v_P^2 - v_S^2\right)} \quad (7)$$

where E_d is dynamic Young's modulus, ρ is density of the studied sample, v_s is S-wave velocity, v_p is P-wave velocity, G_d is dynamic shear modulus, ν is Poisson's ratio.

The calibration of the piezosensors was undertaken using radiation through three steel cylinders of the same class and the lengths 30, 60, and 90 mm. The delay of the wave on the piezosensors was calculated using linear regression and subtracted from all measurements. For P-waves it was 0.273 μs, for S-waves 0.253 μs. The measurement error was specified by repeated radiography of randomly chosen

Table 2 The chemical composition of the rocks within the KZ-25 borehole (Hanák et al., 2010).

Rock Type	K-alkali feldspar syenite	leucogranite	leucogranite	leucogranite	leucogranite	alkali feldspar syenite
Depth [m]	18.8m	26.4m	36m	58.7m	75.5m	101.2m
SiO_2	62.80	78.12	75.90	77.92	74.48	69.54
TiO_2	0.03	0.02	0.04	0.03	0.04	0.03
Al_2O_3	19.84	12.43	13.64	12.34	14.05	17.06
Fe_2O_3	0.04	0.04	0.04	0.07	0.17	0.07
FeO	0.16	0.16	0.20	0.20	0.22	0.11
MgO	0.05	0.07	0.06	0.08	0.05	0.04
MnO	0.03	0.03	0.03	0.04	0.06	0.04
CaO	0.40	0.33	0.38	0.42	0.37	0.43
Li_2O	0.06	0.04	0.05	0.05	0.04	0.03
Na_2O	3.90	4.16	4.23	4.52	4.43	5.79
K_2O	10.06	2.54	4.01	2.50	4.25	5.18
P_2O_5	0.67	0.31	0.38	0.33	0.41	0.51
F	0.33	0.23	0.23	0.18	0.20	0.17
Ign. loss	0.80	0.78	0.50	0.57	0.44	0.54
$H_2O(-)$	0.12	0.12	0.05	0.07	< 0.05	0.10
F(ekv)	-0.14	-0.10	-0.10	-0.08	-0.09	-0.07
Total [%]	99.28	99.38	99.74	99.31	99.23	99.64

samples. The error was 0.8 % for P-waves and 1.3 % for S-waves.

3.6. DEFORMABILITY IN UNIAXIAL COMPRESSION

This method determines the elastic parameters of rock. The cylindrical samples (50x100 mm) were loaded with uniaxial stress. During the experiment, both the transverse and longitudinal deformation of the samples was recorded by resistivity tensometers (20/120LY41 Hottinger Baldwin Messtechnik) attached to the surface of the sample. The loading was implemented in five cycles with a constant gradient of axial stress of 0.5 MPa.s^{-1}. The loading maxims were 20, 30, 40, 50, and 60 % of compressive strength while the unloading minimum was set to 5 % of the compressive strength. Static Young's modulus and Poisson's ratio were calculated following the methods of Zavoral et al. (1987). Static Young's modulus E and Poisson's ratio ν were determined from the hysteresis of the first and second loading loop (Eq. 8, 9).

$$E = \frac{\sigma_{1,3} - \sigma_{2,5}}{\frac{\varepsilon_{a1} - \varepsilon_{a3}}{2} - \varepsilon_{a2}} \tag{8}$$

$$\nu = \frac{\frac{\varepsilon_{d1} + \varepsilon_{d3}}{2} - \varepsilon_{d2}}{\frac{\varepsilon_{a1} + \varepsilon_{a3}}{2} - \varepsilon_{a2}} \tag{9}$$

where ε_{ai} and ε_{di} are appropriate average values of longitudinal and transverse deformation respectively, $\sigma_{1,3}$ and $\sigma_{2,5}$ are maximal and minimal values of corresponding loading and unloading stresses. Finally, the uniaxial compressive strength was determined as proposed by ISRM (1979).

3.7. SCANNING ELECTRON MICROSCOPY

Nine polished symplex were studied using a scanning electron microscope (Quanta 450).The polished samples were made in orientation perpendicular to the borehole KZ-25. Following the fissure distribution plans, the fragments and polished samples were studied in their natural state and coated with gold. The secondary (SE) and backscattered (BSE) electron detectors were used for taking photographs of each sample. The SE mode is the most important because these electrons can be collected easily using a positively biased collector grid placed on one side of the specimen due to the low exit energy of a few electronvolts. Unlike SE, BSE move on straight trajectories and are not affected by electrostatic collection fields (Reimer, 1998).

Table 3 The connected porosities (n_{IRSM}, n_{hc}), mercury porosimetry (n_{Hg}), total porosity (n_T), hydraulic conductivity, and dry density.

Depth [m]	n_{IRSM} [%]	n_{hc} [%]	n_{Hg} [%]	n_T [%]	Hydraulic conductivity [m.s^{-1}]	Dry density [kg.m^{-3}]
18	1.61	1.77	1.04	2.26	1.65×10^{-10}	2510
28	2.00	2.10	2.24	3.16	1.40×10^{-10}	2540
38	1.89	2.08	1.90	2.61	1.30×10^{-11}	2560
48	0.86	0.95	1.27	2.12	1.15×10^{-11}	2585
58	1.34	1.59	1.74	3.24	9.52×10^{-12}	2568
76	0.55	0.65	1.05	1.96	1.01×10^{-12}	2564
88	0.59	0.67	1.94	2.63	2.33×10^{-12}	2563
98	0.45	0.56	0.92	2.33	3.16×10^{-12}	2552
108	0.40	0.54	0.73	2.06	7.80×10^{-13}	2600

Table 4 The velocities of P-waves (Vp) and S-waves (Vs) of unsaturated, saturated, and dry samples.

Depth [m]	Vp uns [m.s^{-1}]	Vs uns [m.s^{-1}]	Vp sat [m.s^{-1}]	Vs sat [m.s^{-1}]	Vp dry [m.s^{-1}]	Vs dry [m.s^{-1}]
18	4173	2569	5564	2870	4031	2557
28	4251	2809	5308	3022	4148	2641
38	4577	2957	5357	3157	4582	2900
48	5151	3254	5763	3345	4899	3093
58	4830	3163	5415	3621	4867	3228
76	5267	3293	5810	3635	5225	3267
88	5441	3393	5786	3511	5194	3237
98	5446	3325	5910	3517	5329	3348
108	5441	3475	5830	3485	5361	3368

Nine samples were taken from distinct depth levels. The morphology and structure of each of the pore networks were described using identical microscope settings: a detector with backscattered electrons, beam current 30.00 kV, working distance 10 mm, spot 8, and magnification 74x. The pore network was drawn manually from the highest applicable magnification in Corel Draw software. The number of pores and fractures were then counted. The final pictures were compiled by QuantumGIS software and the relative directions of the fractures were computed in MapInfo software. In addition, the specific types of microfractures and pores were investigated using the scanning electron microscope and variable magnifications of up to 5000x. More than 100 detailed photographs of the samples were taken to document the microfractures.

4. RESULTS

4.1. SAMPLING AND CHEMICAL ANALYSIS

The most common rocks within the KZ-25 borehole are leucogranite and alkali feldspar syenite (Table 1). The studied granite has enhanced amounts of albite and K-feldspar but average amounts of quartz. This type of granite is characterised by small amount of dark minerals, especially micas in this case. Table 2 presents the chemical composition of the rocks within the borehole. The average volume of SiO_2 is about 70 wt %. The leucogranite samples contain more than 70 wt % SiO_2, 12-14 wt % Al_2O_3, and 2-4 wt % K_2O and Na_2O.

4.2. CONNECTED AND TOTAL POROSITY

The connected porosity of the samples describes the pores and fractures that are accessible by water whereas the total porosity also includes isolated voids and microfractures. Therefore, the total porosity should be greater than the connected porosity. The connected porosities n_{ISRM} and n_{hc} were both calculated using same equation but with different weights of saturated sample depending on the method used. It is seen that the connected porosity n_{hc} is greater than n_{ISRM} in all samples. (Table 3). The connected porosity is somewhat depth dependent with the highest connected porosity in the sample from 28 m and the lowest in the sample from 108 m. The total porosity was found to be highest in the sample from 58 m and lowest in the sample from 76 m. There is no correlation between the connected and total porosities (Table 3).

4.3. MERCURY POROSIMETRY

The higher values recorded by Hg porosimetry reflect the fact that the measurements have been

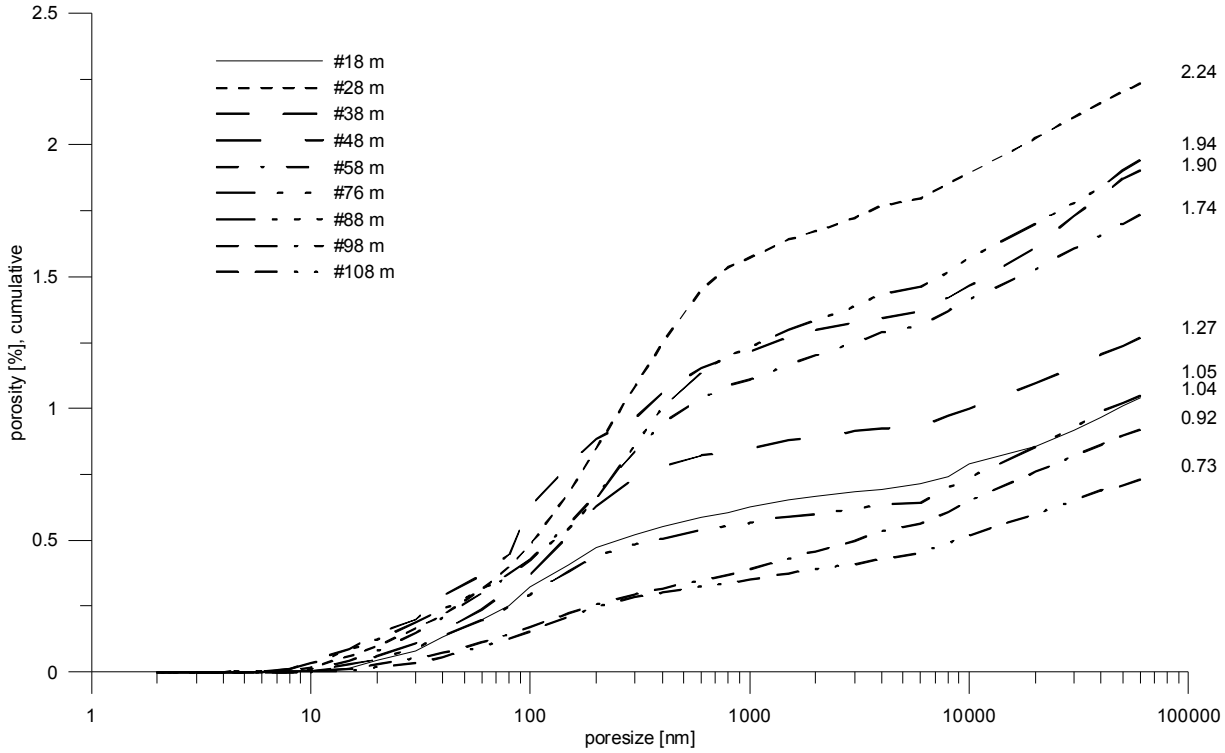

Fig. 6 The pore size distribution according to the mercury porosimetry.

Table 5 Young's modulus (Edyn), shear modululus (Gdyn) and Poisson's ratio (ν) of unsaturated, saturated, and dry samples.

Depth [m]	Edyn unsat. [GPa]	Gdyn unsat. [GPa]	ν dyn unsat. [-]	Edyn sat. [GPa]	Gdyn sat. [GPa]	ν dyn sat. [-]	Edyn dry [GPa]	Gdyn dry [GPa]	ν dyn dry [-]
18	39.58	16.56	0.19	54.52	20.67	0.32	38.19	16.41	0.16
28	44.59	20.05	0.11	58.45	23.19	0.26	41.06	17.71	0.16
38	51.12	22.38	0.14	62.97	25.51	0.23	50.20	21.53	0.17
48	63.93	27.37	0.17	72.07	28.93	0.25	57.80	24.73	0.17
58	57.78	25.69	0.12	73.77	33.67	0.10	59.25	26.75	0.11
76	65.55	27.80	0.18	79.84	33.88	0.18	64.52	27.36	0.18
88	69.73	29.50	0.18	76.37	31.60	0.21	63.51	26.85	0.18
98	67.87	28.22	0.20	77.38	31.56	0.23	67.15	28.60	0.17
108	72.54	31.39	0.16	77.16	31.57	0.22	69.23	29.48	0.17

obtained using high pressure in addition to the comparatively high influence exerted by the open surface pores. The only exceptions come from the samples at 18 m and 38 m, in which the Hg porosimetry is lower by almost 30 %. The highest porosity is associated with the sample from 28 m (Table 5), in accordance with that found by other methods. In general, the pore size distribution demonstrated by mercury porosimetry is characteristically similar for all of the samples irrespective of depth (Fig. 6). This trend is, however, impaired by the increases in porosity seen in the samples from 58 and 88 m. The cumulative curves in a semi-logarithmic scale show two clear breakpoints. The first occurs between 200 and 500 nm while the second occurs at about 7000 nm. Figure 6 also suggests that the measured mercury porosity is significantly influenced by pores of less than 500 nm. The contribution of these pores into the sample porosity ranges between 0.25 % and 1.71 %. In contrast, the contribution of pores of greater than 500 nm was found to be quite similar for all the samples (between 0.48 % and 0.69 %). Thus, in terms of variability, the influence of the smaller pores is significantly higher.

4.4. HYDRAULIC CONDUCTIVITY AND DRY DENSITY

The hydraulic conductivity corresponds to the depth within the borehole (Fig. 7: middle). The highest value of 1.65×10^{-10} m.s^{-1} was measured in the sample from 18 m while the lowest value of 7.80×10^{-13} m.s^{-1} was in the sample from 108 m

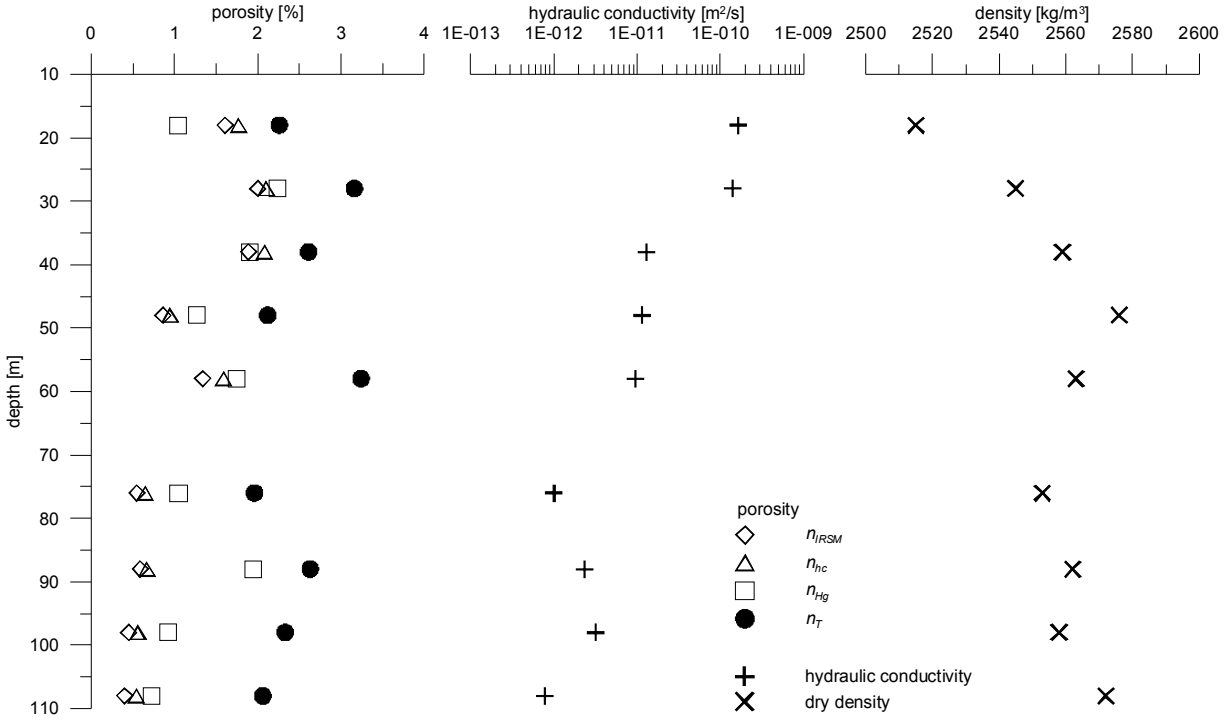

Fig. 7 The porosity (left), hydraulic conductivity (middle), and dry density (right) to depth relationships.

Table 6 The deformation parameters.

Depth [m]	Static Young's modulus [GPa]	Poisson's ratio [-]	Uniaxial compressive strength [MPa]	Moisture [%]
48	49.2	0.24	118	0.15
58	50.5	0.24	142	0.19
98	59.9	0.23	161	0.12
108	56.6	0.19	105	0.13

(Table 3). The dry density shows the opposite patterns in top 50 metres, as these values increase with depth. In the deeper part, there is no clear trend (Fig. 7: right). The lowest value of 2510 kg.m^{-3} was calculated in the sample from 18 m while the greatest value of 2600 kg.m^{-3} was calculated in sample from 108 m (Table 3). Any way there is an increasing trend between 18 m and 48 m and an opposite trend between 48 m and 98 m.

4.5. ULTRASONIC VELOCITIES

The results of the ultrasonic measurements of P-waves and S-waves for unsaturated, saturated, and dried samples are shown in Figure 8. P-wave velocities vary from 4173 m.s^{-1} to 5446 m.s^{-1} in the unsaturated samples, from 5308 m.s^{-1} to 5910 m.s^{-1} in the saturated samples, and from 4031 m.s^{-1} to 5361 m.s^{-1} in the dry samples (Table 6). The lowest velocities were measured in samples from 18 m and 28 m while the highest velocities were measured in the samples from 98 m and 108 m. The velocities broadly increase with depth (Fig. 8). S-wave velocities vary from 2569 m.s^{-1} to 3475 m.s^{-1} in the unsaturated samples, from 2870 m.s^{-1} to 3635 m.s^{-1} in the saturated samples, and from 2557 m.s^{-1} to 3368 m.s^{-1} in the dry samples (Table 6). The lowest velocities were again measured in sample from 18 m while the highest velocities were measured in the samples from 98 m and 108 m (although, in the saturated samples, this was in the sample at 76 m). Nonetheless, the velocities again broadly increase with depth (Fig. 8).

All moduli were calculated using Equations 4 and 5. Dynamic Young's modulus, dynamic shear modulus, and Poisson's ratio were calculated for the unsaturated samples, saturated samples, and dry samples. There are significant differences between moduli of the saturated samples compared to those of the unsaturated and dry samples (Table 7). Dynamic Young's modulus for the unsaturated samples varies from 39.58 GPa to 72.54 GPa, for the saturated samples it varies from 54.52 GPa to 79.84 GPa, and for the dry samples it varies from 38.19 GPa to 69.23 GPa (Table 5). The lowest values were calculated in the sample from 18 m while the highest come in the samples from 76 m or 108 m. The highest

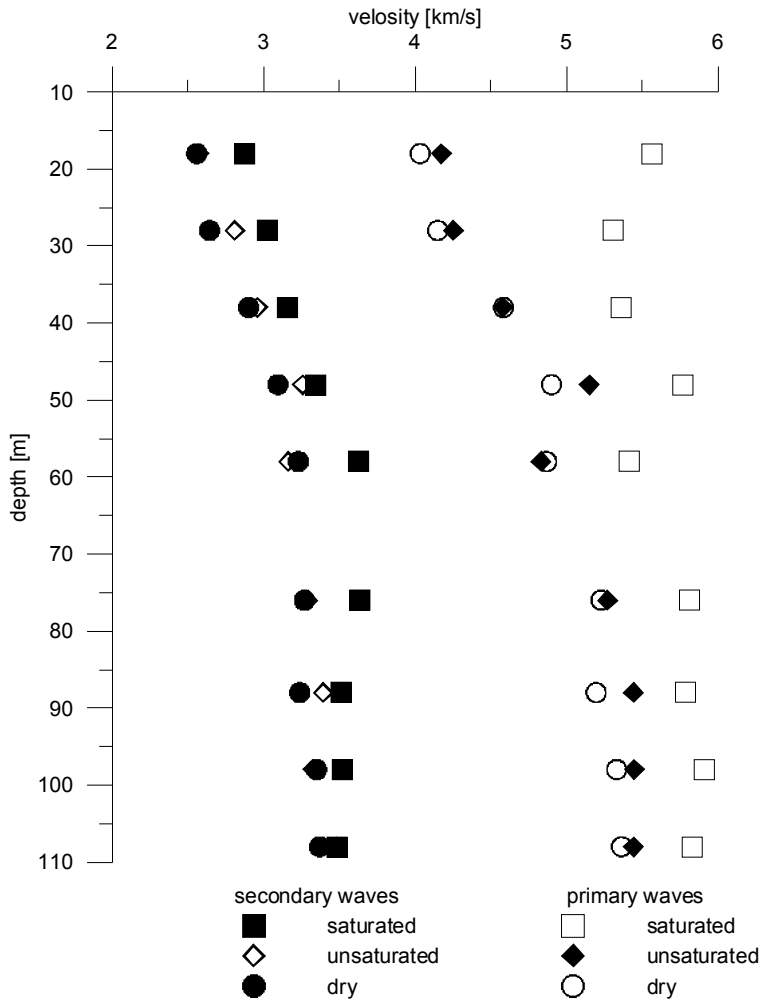

Fig. 8 The P-wave and S-wave velocities to depth relationship.

Table 7 Number of fractures and pores and their physical characteristics observed in polished samples from borehole KZ-25.

Depth [m]	Number of fractures	Number of pores	Total	The shortest fracture [μm]	The longest fracture [μm]	The narrowest fracture [μm]	The widest fracture [μm]	Total length of fractures [mm]
18	30	602	632	78.80	448.20	1.17	10.07	12.10
28	78	703	781	3.05	605.40	0.49	19.69	29.04
38	128	1252	1380	10.20	461.90	0.75	62.30	26.62
48	90	901	991	20.62	976.40	1.01	74.54	16.94
58	109	1538	1647	3.85	668.00	0.58	54.88	17.77
76	58	1061	1119	3.07	1795.00	1.27	45.68	11.64
88	121	1437	1558	4.72	668.80	0.52	46.04	21.33
98	88	864	952	19.25	717.40	0.93	45.37	16.26
108	65	911	976	55.67	1847.00	9.64	72.48	12.26

dynamic Young's modulus of saturated samples was calculated at 76 m. The values of the moduli increase with depth in the studied borehole (Fig. 9).

Dynamic shear modulus for the unsaturated samples varies from 16.56 GPa to 31.39 Pa, for the saturated samples it varies from 20.67 GPa to 33.88 GPa, and from the dry samples it varies from 16.41 GPa to 29.48 GPa (Table 5). Poisson's ratio for the unsaturated samples varies from 0.11 to 0.20, for the saturated samples it varies from 0.10 to 0.32, and for the dry samples it varies from 0.11 to 0.18 (Table 5). The lowest values were calculated in the samples from 28 m and 58 m while the highest values were from 98 m or 108 m. Figure 9 shows the

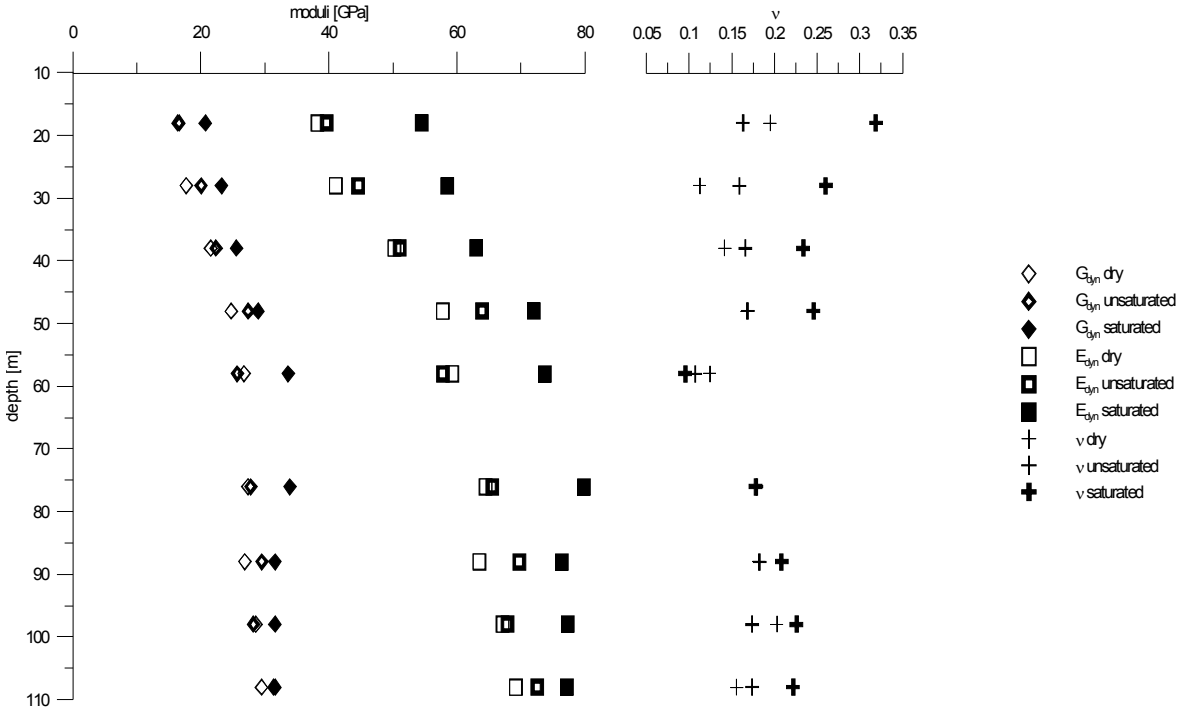

Fig. 9 Young's modulus (Edyn), shear modululus (Gdyn) and Poisson's ratio (ν) to depth relationship.

progression of all moduli and Poisson's ratio within borehole.

4.6. DEFORMABILITY IN UNIAXIAL COMPRESSION

Samples from 48, 58, 98, and 108 m were chosen in order to test their deformability. Due to lack of other samples it was not possible to perform the other tests. The static Young's modulus, Poisson's ratio, uniaxial compressive strength and moisture were calculated by these tests. Static Young's modulus generally increases with depth and varies from 49.2 GPa to 59.9 GPa. Poisson's ratio varies from 0.24 to 0.19 and decreases between 98 and 108 m. The highest compressive strength was measured in the sample from 98 m while the lowest was measured in the sample from 108 m (Table 6).

4.7. SCANNING ELECTRON MICROSCOPY

Figure 10 presents the SEM images from all the sampled depth levels. The three most common minerals are visible: quartz (dark grey, high relief); albite (dark grey, low relief); and K-feldspar (light grey). The images reveal the distribution of pores and microfractures in the granite. It appears that the majority of the pores and fractures occur in both albite and K-feldspar. The manually marked pore networks on the images (Fig. 11) documents, that pores and fractures are variously distributed within the rocks. A numer of fractures attain lengths of more than 1 mm (Figs. 10 a, b, c, f, h, i) and there is a network of interconnecting microfractures. The pore distribution does not appear to be depth dependent and may vary markedly within a given sample. The greatest numbers of pores occur in the sample from 38 m while the greatest numbers of fractures occur in the sample from 58 m. The least numbers of pores and fractures occur in the sample from 18 m (Table 7). The grain boundaries and minerals have been distinguished (Fig. 11) while the fractures and pores distributed in the minerals have been counted (Table 8). The highest grain boundary pore ratio occurs in the sample from 48 m.

Illustrative views of the distribution of the pores and fractures within the borehole are presented in Figure 12 and 13. The relative direction of the various fractures was computed in MapInfo software. The rose diagrams were displayed in Tectonics_FP software. Figure 14 presents rose diagrams of the microfractures at different depths. It should be noted that these are not actual directions. There are two distinct orthogonal fracture sets in the granite samples from borehole KZ-25. Two sets of faults have also been found in granites in NE part of the Bohemian Massif (Nováková, 2008). The narrowest fracture with a width of 0.49 μm was found in the sample from 28 m while the widest fractured with a width of 74.54 μm was found in the sample from 48 m (Table 7). Measuring the length of the fractures is problematic due to the small visible area seen by the microscope. Nevertheless, the shortest fracture was measured in the sample from 28 m while the longest was in the sample from 108 m (Table 7).

5. DISCUSSION

There has been much recent attention directed towards the properties of granite matrix. A number of papers have used local granites to investigate

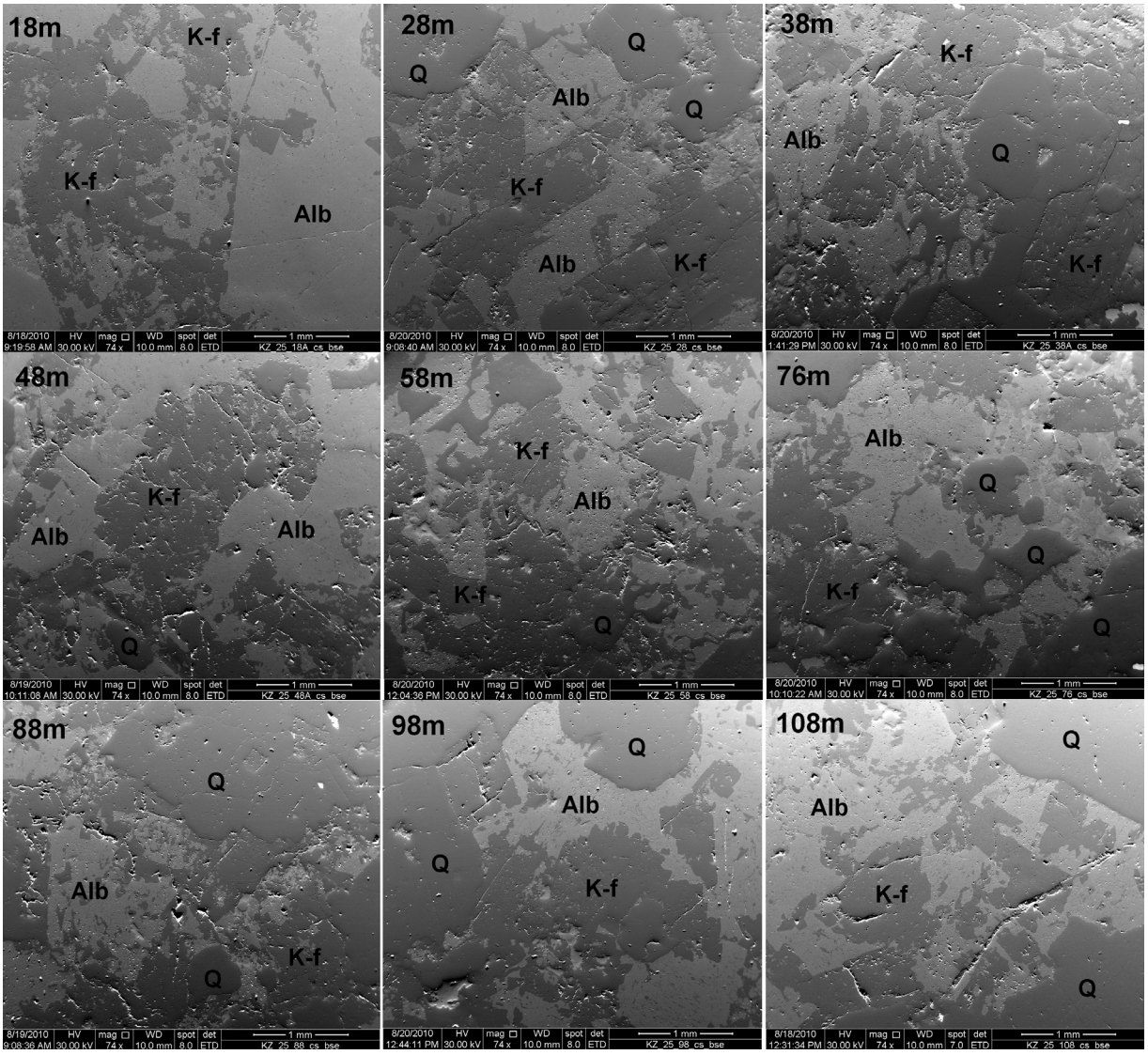

Fig. 10 SEM-microphotographs of polished surface of granite samples from borehole KZ-25. Q: Quartz, K-f: K-feldspar, Alb: Albite.

Table 8 Number of fractures and pores in the minerals. GBP-Grain boundary pores, fract.-fractures.

Depth [m]	Albite					K-feldspar					Quartz					GBP
	pores	/mm^2	fract.	/mm^2	area	pores	/mm^2	fract.	/mm^2	area	pores	/mm^2	fract.	/mm^2	area	ratio
18	155	10.5	5	0.34	0.59	447	43.4	25	2.42	0.41	0	-	0	-	0.00	0.00
28	223	36.5	6	0.98	0.25	365	27.8	37	2.82	0.52	115	19.9	7	1.22	0.23	2.28
38	499	74.0	5	0.74	0.27	589	47.2	70	5.62	0.50	165	28.4	17	2.93	0.23	2.15
48	238	19.9	11	0.92	0.48	619	53.0	66	5.65	0.47	44	32.5	2	1.49	0.05	8.68
58	587	63.0	6	0.64	0.37	909	68.2	83	6.23	0.53	42	18.0	2	0.85	0.09	5.69
76	491	51.3	5	0.52	0.38	420	46.5	38	4.20	0.36	150	23.4	5	0.78	0.26	1.41
88	397	65.3	1	0.16	0.24	678	61.8	68	6.20	0.44	362	45.5	21	2.64	0.32	1.38
98	172	21.7	6	0.76	0.32	509	52.7	54	5.59	0.39	183	24.7	14	1.89	0.30	1.31
108	433	40.2	10	0.93	0.43	375	44.0	41	4.81	0.34	103	18.0	6	1.05	0.23	1.49

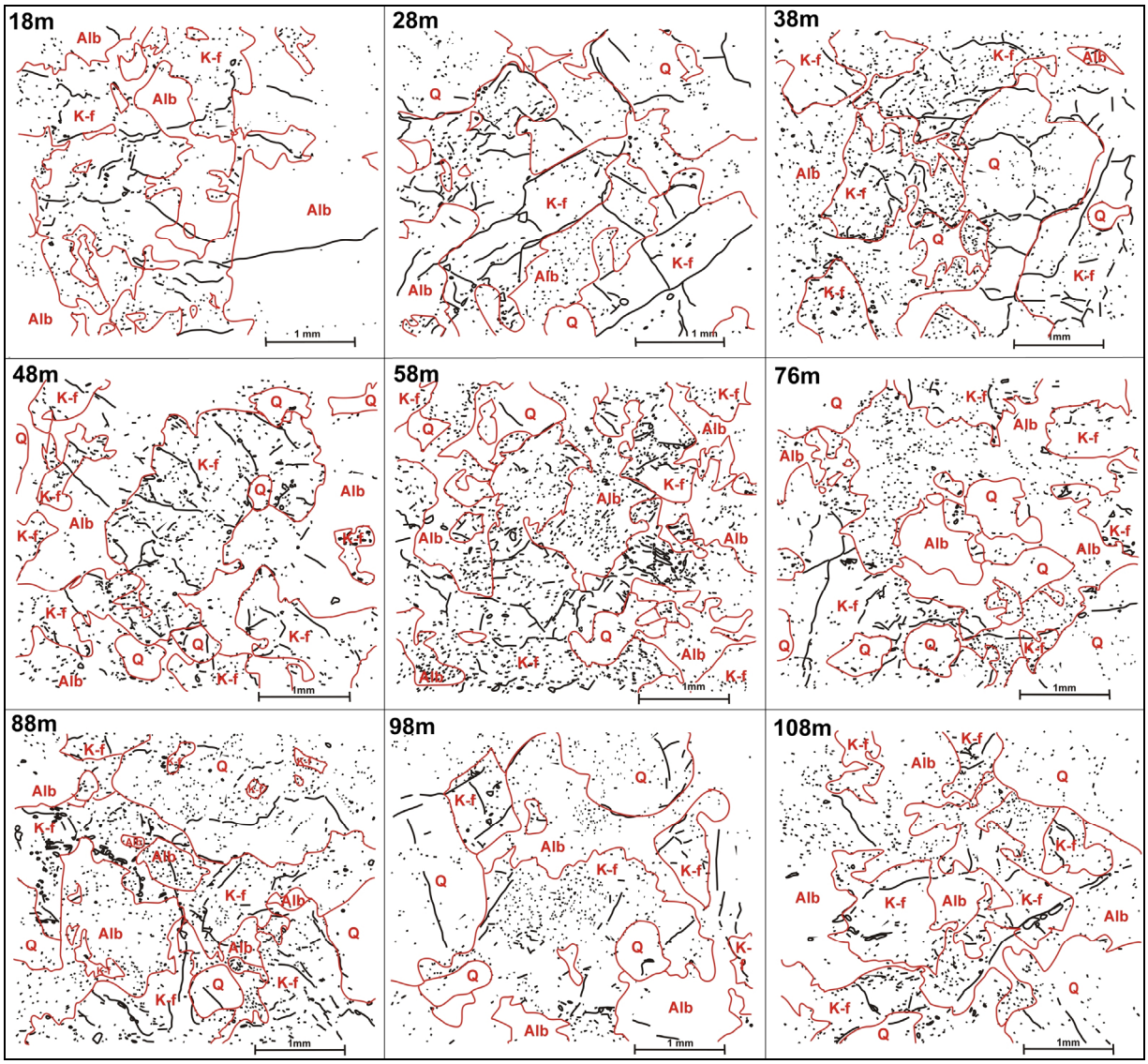

Fig. 11 Manually marked pore and microfracture networks and grained boundary with minerals in granite samples from borehole KZ-25. Q: Quartz, K-f: K-feldspar, Alb: Albite.

microfracturing, porosity, and hydraulic conductivity (e.g. David et al., 2000; Begonha and Sequeira Braga, 2002; Möri et al., 2003; Lion et al., 2005, Nováková et al., 2011). Unless it forms part of a comprehensive project into, for example, the feasibility of a nuclear waste repository, these papers usually focus on a specific parameter which is studied by a single method or a set of closely related methods.

In this study, the porosity has been obtained using three different methods. A comparison of these measured porosities shows that average value of n_{ISRM} is 1.08 % while average n_{hc} is 1.21 % (Table 5). This suggests that some air bubbles remained inside the samples even after a long period of saturation under vacuum. During the hydraulic conductivity test, the remaining air was expelled and therefore n_{hc} gives greater values than n_{ISRM}. Even higher values were obtained from mercury porosimetry with a mean average of 1.43 %. These n_{Hg} values may be explained by the size of the samples because more of the originally isolated microcracks are accessible from the surface in smaller samples. It is possible that mercury porosimetry overestimates the porosity as the results may be affected by the surface roughness of the samples (Onishi and Shimizu, 2005). The estimation of the total porosity n_T gives a significantly higher value than that of open porosity, with an average of 2.49 %. It may be that significant part of the total porosity occurs within an interconnected network determined after hydraulic conductivity test. Despite these differences, the obtained porosities follow the same trends irrespective of the actual method applied. The connected porosity should depend on the rock type, in particular its chemical or mineralogical composition and fabric. The sample from the depth of 26.4 m contains 78 wt % SiO_2, which is the highest recorded content within the borehole (Table 2).

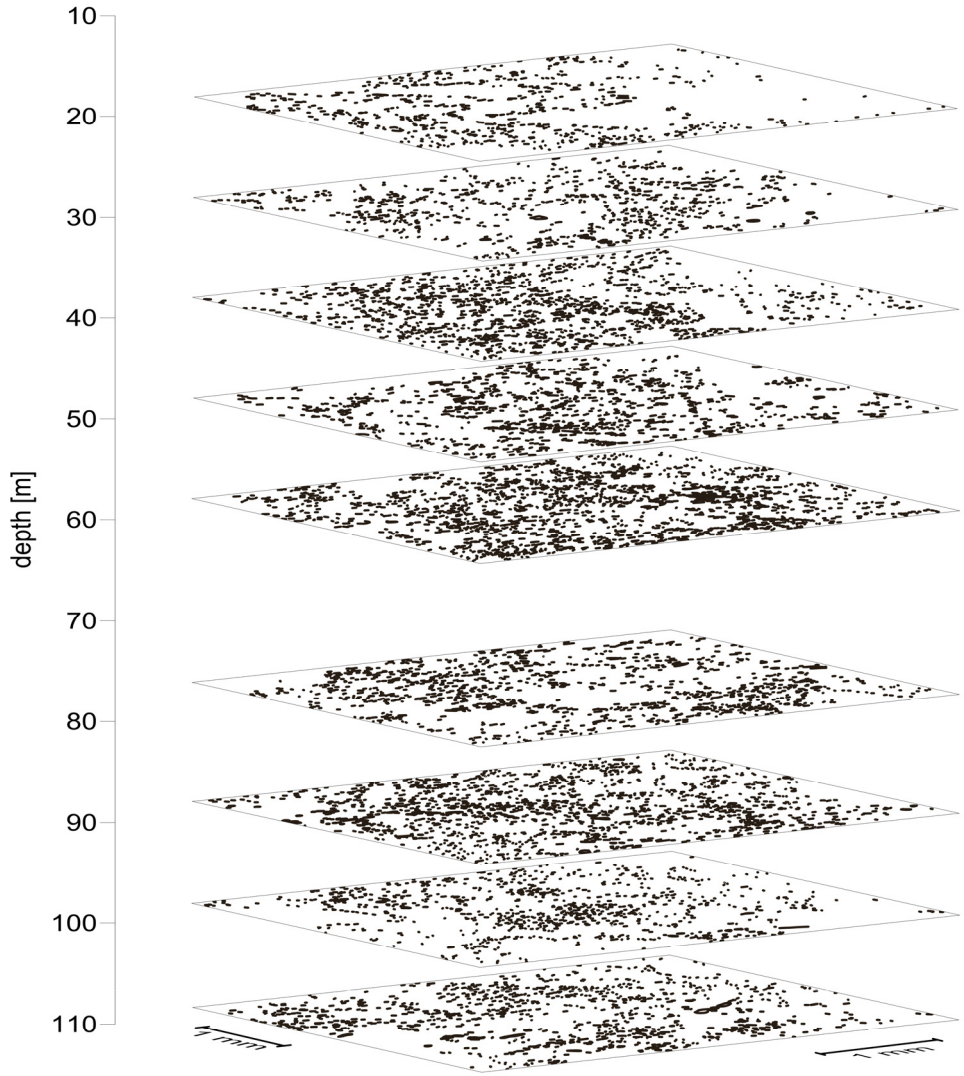

Fig. 12 Manually marked pore networks in granite samples from borehole KZ-25.

The higher porosity values obtained by the mercury porosimetry in comparison to the standard methods may result from the use of high pressure during the measurements. However, given the size of the samples and the generally low porosity of the studied granite, the influence of open surface pores also ought to be considered. The mercury porosimetry revealed somewhat atypical characteristics in the pore size distribution in all of the studied samples. The existence of three distinct groups of pores is indicated by breakpoints on the curves. The real size of these pores and fractures, supposed to be as wide as 7000 nm, was also found by the SEM. It may be that these features in fact represent open surface pores induced during sampling and preparatory work. Furthermore, the porosity measured by the mercury porosimetry corresponds far more closely to those obtained by the other methods after excluding pores over 7000 nm. It is only possible to speculate as to whether the remaining two groups represent genuine categories of fractures and pores.

A completely different perspective on matrix porosity is provided by the SEM. The manual tracing of pores and fractures is somewhat subjective. It does, nevertheless, provide useful spatial and structural information (Nováková et al., 2010). In order undertake further geological analyses, it is necessary to know the orientation of the samples. This is simply not known for the analysed core. During the original survey no borehole logging methods were applied that could have been used to orientate the core later. Furthermore, due to quarrying, the location of the KZ-25 borehole does not exist anymore. Despite this problem, the SEM images show the density and structure of both pores and microfractures with up to three significant microfracture directions identified. The information regarding the connectivity between fractures provided by the SEM is important for future

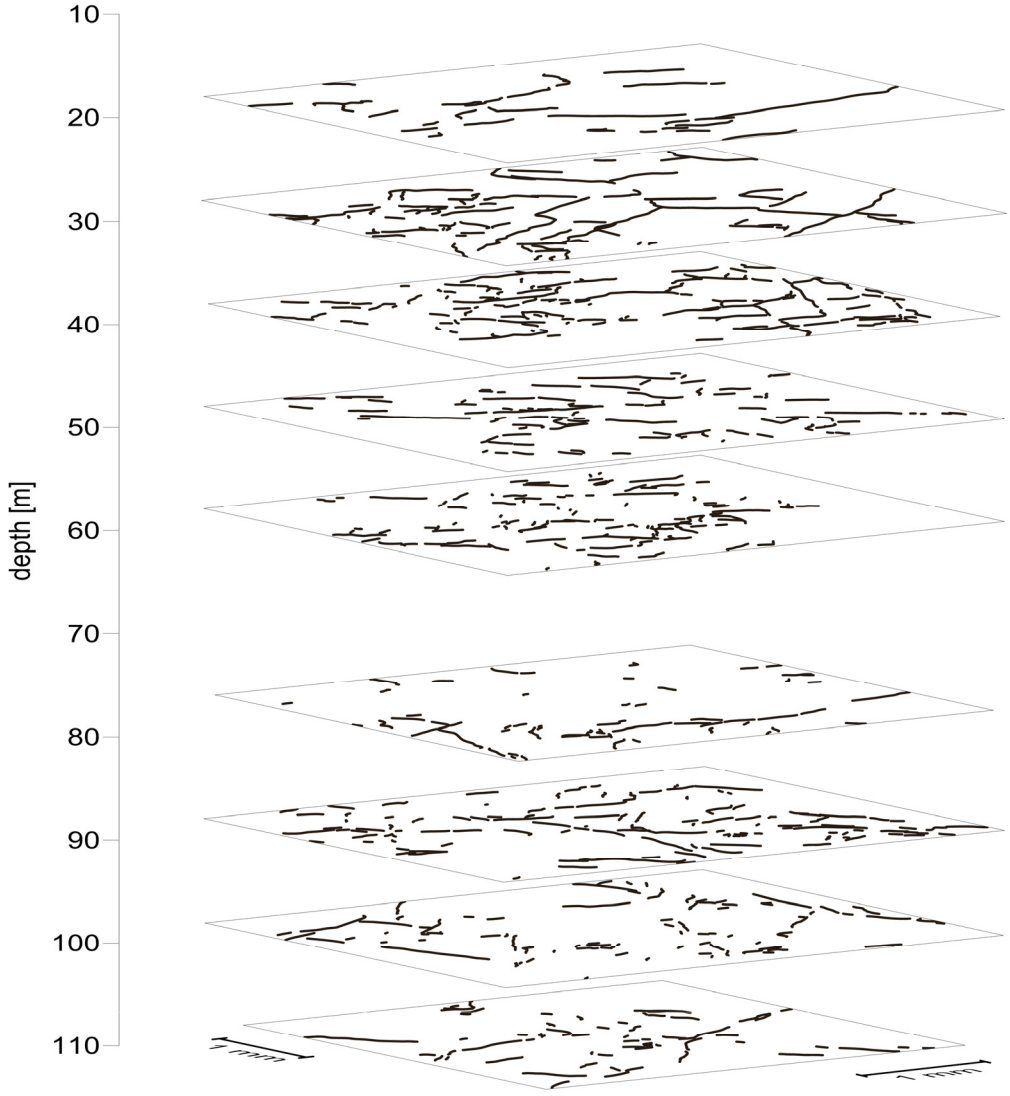

Fig. 13 Manually marked microfracture networks in granite samples from borehole KZ-25.

modelling. The process of manual tracing is more precise than the automated drawings generated by special programs although it is clearly time consuming (Machek, 2011).

Möri et al. (2003) defined four types of granite matrix pores: grain boundary pores, sheet silicate pores, solution pores, and crack pores. These types have all been identified in the SEM images from borehole KZ-25. However, after careful consideration, for the purpose of investigating the granite matrix we prefer to define the structures as either pores or microfractures. The former are defined as three-dimensional cavities within the matrix while the latter are broadly planar gaps. This division allows an integrated approach based directly on pore shape.

There is no clear linear depth dependence in relation to the number or length of pores and microfractures (Fig. 12 and Fig. 13). The narrowest fractures mapped from the SEM images were estimated to have widths of around 500 nm. Therefore, only the major microfractures were depicted. In addition, this corresponds to a breakpoint indicated by the mercury porosimetry (Fig. 6). The pores mapped from the SEM images represent the smallest category shown by the mercury porosimetry. Nevertheless, a significant proportion of the microfractures may still have been neglected. It is also necessary to note that the dimensions of most of the microfractures measured from the SEM images are apparent, as these microfractures occur at various angles to the image plane.

The highest density of microfractures was found in K-feldspar (between 2.42 and 6.23 microfractures per square millimetre) while the lowest was found in albite (between 0.16 and 0.96). Quartz grains bear between 0.78 and 2.93 microfractures per square

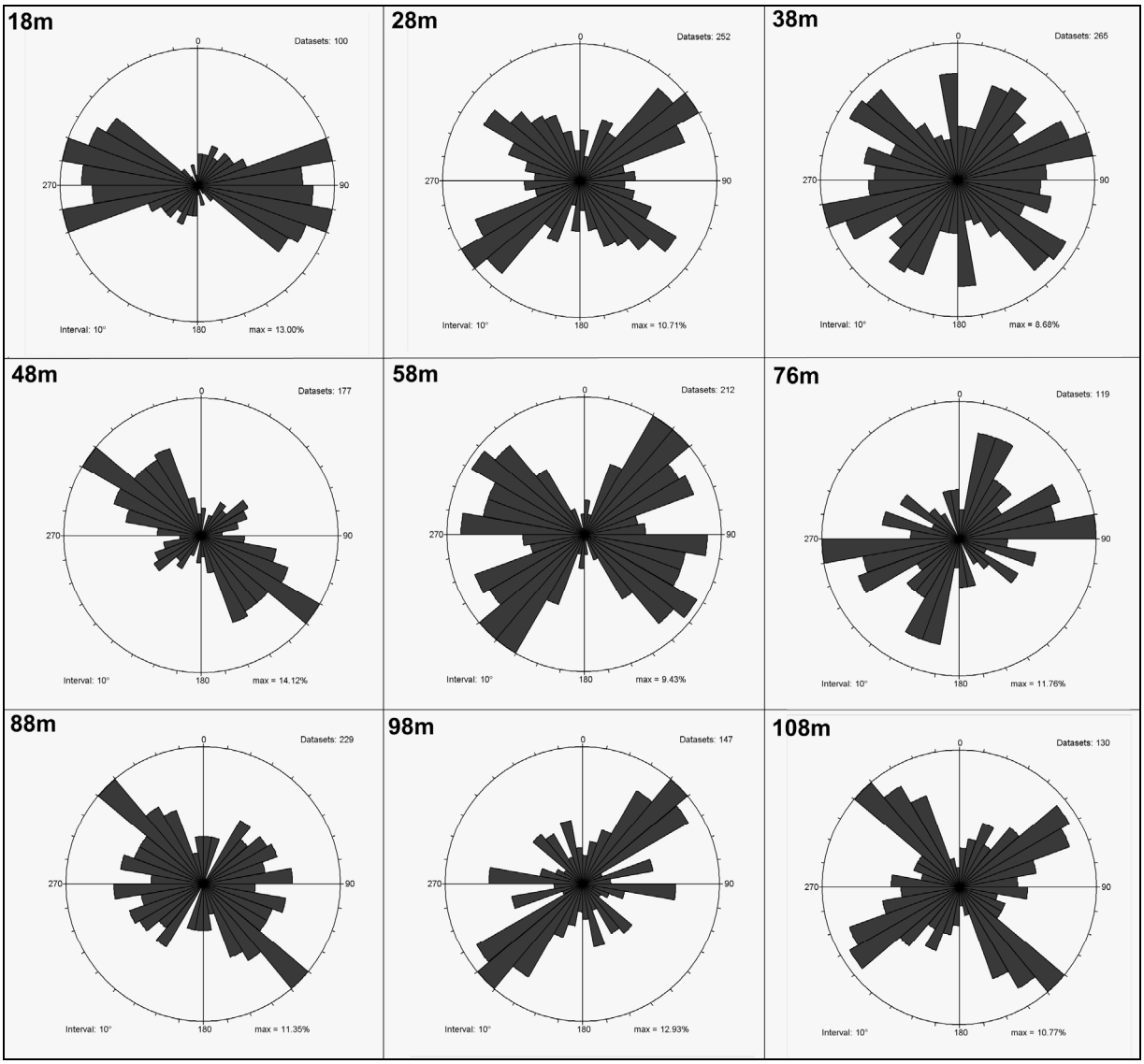

Fig. 14 Rose diagrams of microfractures in granite samples from borehole KZ-25.

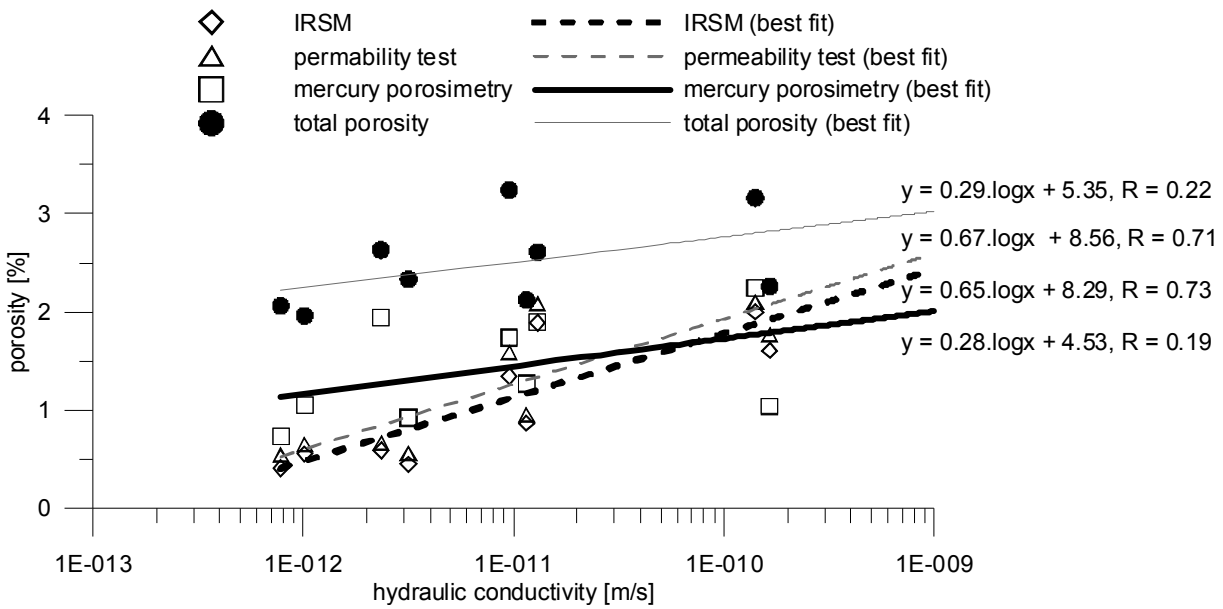

Fig. 15 The relationship between porosities and hydraulic conductivity.

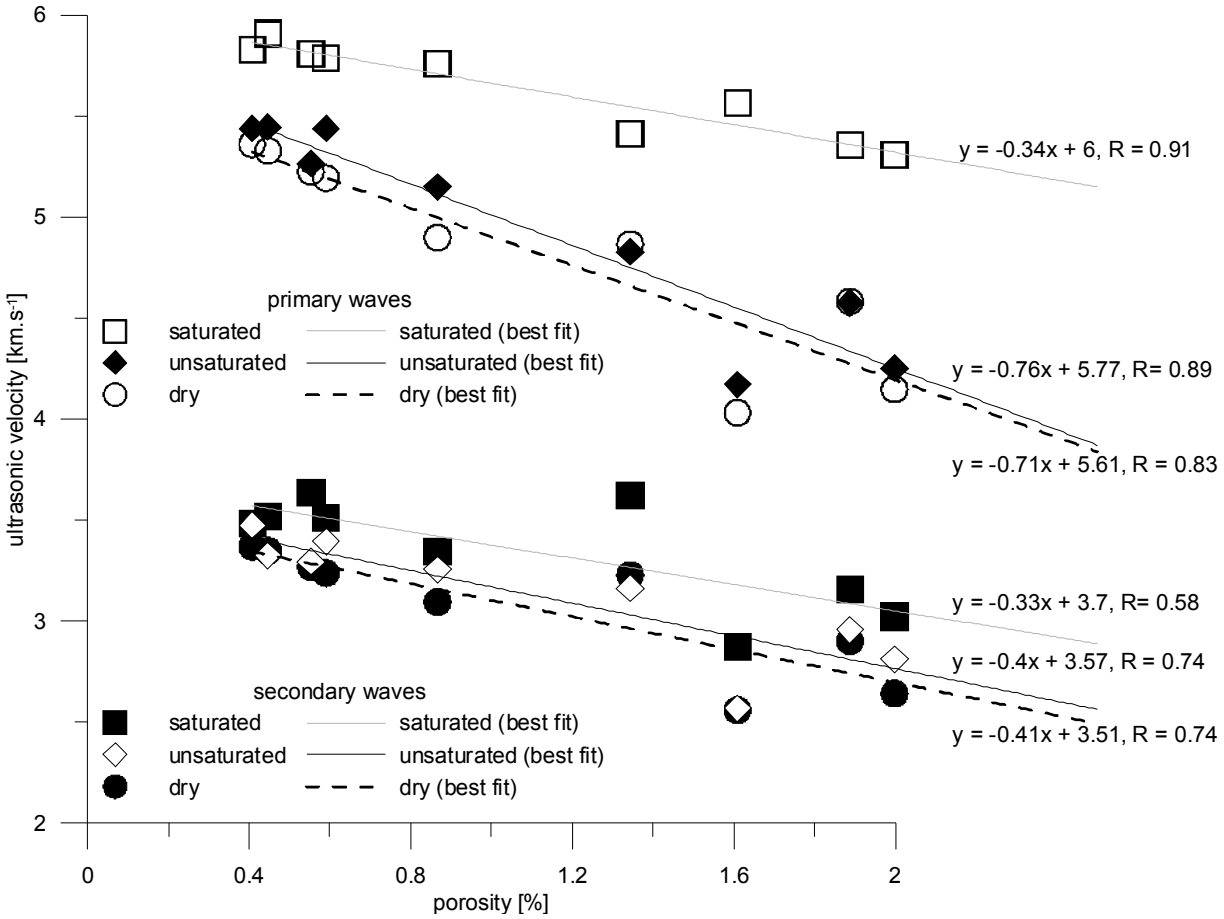

Fig. 16 The relationship between ultrasonic velocities and connected porosity (n_{ISRM}).

millimetre (Table 8). The 28 m sample also demonstrates that the length and connectivity of the microfractures is important. A relatively low number of well connected long fractures contribute significantly to the hydraulic conductivity. Mori et al. (2003) stated the most important contributor to granite matrix porosity were tiny fractures that followed grain boundaries, called grain boundary pores. The grain boundary pores form up to 40 % of all microfractures in the matrix. Moreover, the grain boundary pores, where found, were observed to be both long and well connected in the KZ-25 granite (Fig. 11).

There is an ambiguous relationship between porosity and depth that has been observed in all the results obtained by the various porosity methods. In contrast, the hydraulic conductivity is clearly depth dependent. The porosity and hydraulic conductivity trends are not always followed down the vertical profile and distinct local anomalies can be seen (see depth intervals 18-28 m; 48-58 m and 88-98 m in Fig. 7). This demonstrates that there is no precise correlation between these two parameters. It may be that the hydraulic conductivity can be influenced by a small proportion of the microfractures as these create preferential drainage pathways inside the sample. Porosity, on the other hand, is a volumetric characteristic and it is influenced by all the microcracks in the measured sample regardless of their contribution to the hydraulic properties. A logarithmic relationship was found to exist between porosity and hydraulic conductivity (Fig. 15). The presented porosity and hydraulic conductivity measurement methods are rather time consuming. It would be useful to have an easy but reliable method that provides rapid results relating to either granite matrix porosity or hydraulic conductivity on large quantity of samples. It is easy to measure ultrasonic velocities in both the field and laboratory. Therefore, it is promising that it may be possible to correlate ultrasonic velocities and porosity (Fig. 16) or hydraulic conductivity (Fig. 17; Najser et al., 2011).

In borehole KZ-25, the velocity of both the primary and secondary waves decrease with an increase in open porosity. A change of 1.6 % (absolute value) in the open porosity is proportionally equivalent to a change of 1.2 $km.s^{-1}$ in the primary wave velocity of the dried samples. Begonha and Sequeira Braga (2002) found a logarithmic correlation between P-waves and open porosity in a weathered granite with porosities of up to 10 %. The ultrasonic

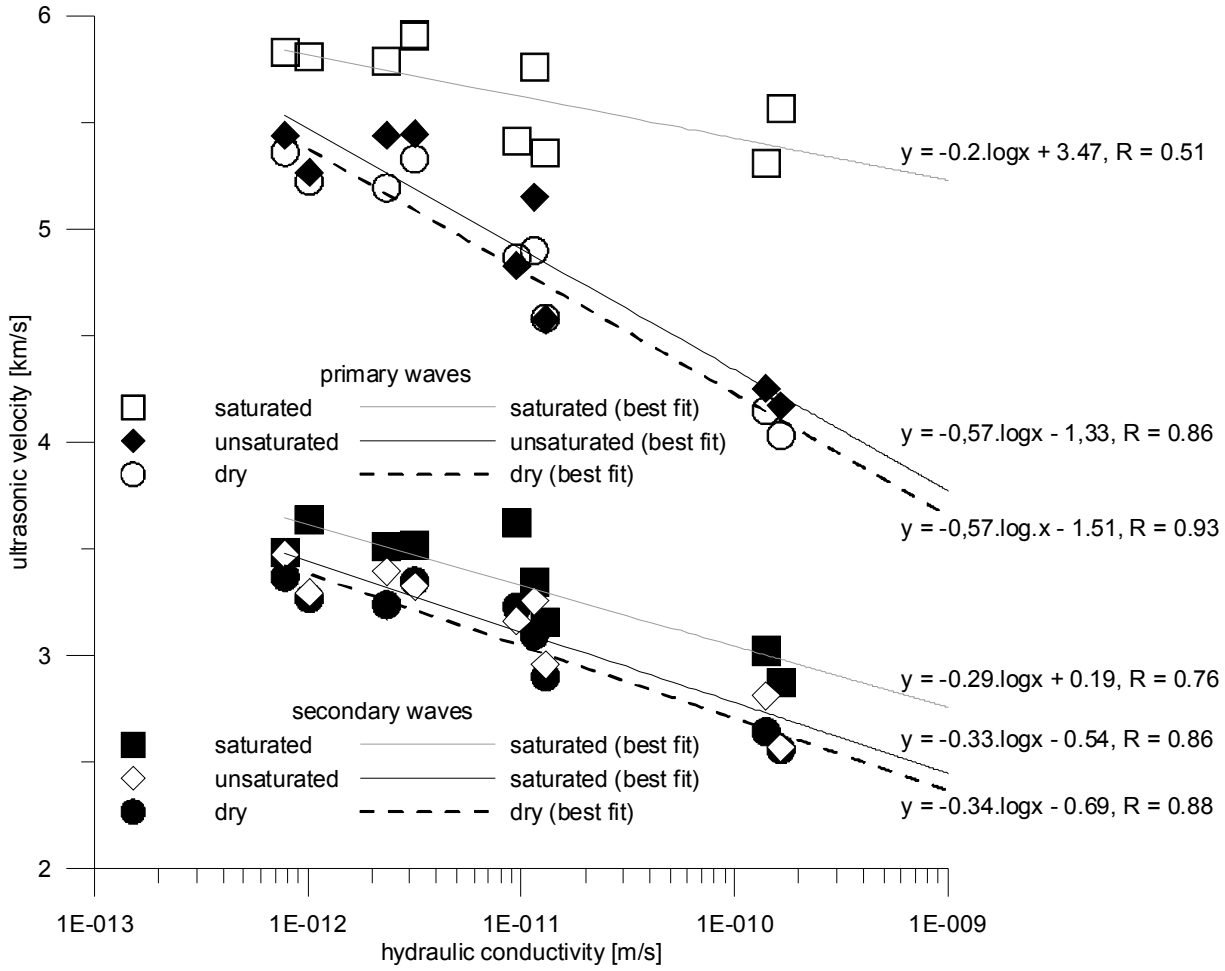

Fig. 17 The relationship between ultrasonic velocities and hydraulic conductivity.

velocities decrease with increasing hydraulic conductivity. The observed relationship is logarithmic. It is in accordance with the observed logarithmic relationship between porosities and hydraulic conductivity.

The laboratory measurements of ultrasonic velocities on dry, saturated, and unsaturated samples gave similar results. The velocities were seen to be very similar in the dry and unsaturated samples whereas v_p were greater in the saturated samples. This comparison shows that dried samples are the most appropriate for ultrasonic velocity measurement. Similar results of the dry and unsaturated samples indicate that the drying process may be omitted eventually for general ultrasonic measurements.

The ultrasonic velocities of both the primary and secondary waves initially increase with depth. However, the measurements of ultrasonic velocities in the samples below about 50 m provided rather uniform results. This may reflect subsurface weathering and therefore the results suggest the KZ-25 granite is weathered to depths of around 50 m. A similar conclusion can be drawn from the density profile presented in Figure 7.

The samples all, with one exception, represent leucogranite (the sample at 18 m is an alkali feldspar syenite). The different mineralogical composition of that sample explains its slightly different behaviour. The majority of the studied parameters correspond with depth (e.g. high hydraulic conductivity, low density, slow ultrasonic velocities, and low values of moduli). The porosity of the sample at 18 m is, however, rather low when compared to the following near surface leucogranite samples and this low porosity was confirmed by the SEM images. It is possible that this reflects a greater amount of interconnected microfractures within the alkali feldspar.

The high porosity samples of the leucogranite come from horizons with slightly higher amounts of SiO_2 and lower amounts of Al_2O_3. The change in the mineralogical composition of the leucogranite again represents a possible explanation.

6. CONCLUSIONS

The various porosimetry methods provided a range of values that followed similar trends. From the recorded data, it is noted that a logarithmic relationship exists between open porosity and hydraulic conductivity. The porosities, ultrasonic velocities, hydraulic conductivities, and bulk densities all show slight depth dependence. The mercury porosimetry showed the typical pore distribution in the studied granite. The mercury porosimetry suggested that some pores are wider than 7000 nm as they were also found by the SEM. The SEM imagery provides a unique view into the granite matrix and the applied resolution made it possible to map microfractures over 0.5 μm. For greater detail, a yet finer resolution is essential. The ultrasonic velocity measurements offer a promising method for indirect porosity and hydraulic conductivity estimation. The most reliable results appear to come from the oven dried samples but the unsaturated samples may be suitable for a rapid general estimation. These data enable us to construct new hypotheses that will now form the basis of the next phase of research into granite matrix porosity.

ACKNOWLEDGMENTS

The project was funded by the Ministry of Industry and Trade of the Czech Republic (Project Number: FR-TI1/367). For their participation, we are grateful to our colleagues at the Czech Geological Survey, Progeo Ltd., and NIR Řež Corp. We would like to thank Dr. M. René for his useful advice and Dr. K. Breiter for the geological description of the core. Thanks are also due to Dr. J. Schweistilová for the SEM, A. Jandečková for the mercury porosimetry analyses, and Z. Fiala for the uniaxial compression tests. Dr. M.D. Rowberry provided a critical review of the English. We also thank to three anonymous reviewers for improvement the manuscript.

REFERENCES

Akesson, U., Hansson, J. and Stigh, J.: 2004, Characterisation of microcracks in the Bohus granite, western Sweden, caused by uniaxial cyclic loading. Engineering Geology 72 (1-2), 131–142.

Begonha, A. and Sequeira Braga, M.A.: 2002, Weathering of the Oporto granite: geotechnical and physical properties. Catena 49 (1-2), 57–76.

Bogner, A., Jouneau, P.H., Thollet, G., Basset, D. and Gauthier, C.: 2006, A history of scanning electron microscopy developments: Towards "wet-STEM" imaging. Micron 38 (4), 390–401.

Chaki, S., Takarli, M. and Agbodjan, W.P.: 2008, Influence of thermal damage on physical properties of a granite rock: Porosity, permeability and ultrasonic wave evolutions. Construction and Building Materials 22 (7), 1456–1461.

David, C., Menéndez, B. and Darot, M.: 2000, Influence of stress-induced and thermal cracking on physical properties and microstructure of La Peyratte granite. International Journal of Rock Mechanics and Mining Sciences 36 (4), 433–448.

Dolníček, Z., René, M., Prochaska, W. and Kovář, M.: 2012, Fluid evolution of the Hub Stock, Horní Slavkov-Krásno Sn-W ore district, Bohemian Massif, Czech Republic. Mineralium Deposita (doi:10.1007/s00126-012-0400-0).

Felch, D.E. and Shuck, F.O.: 1971, Determination of pore-size distribution in porous materials. Test of a proposed method. Industrial and Engineering Chemistry Fundamentals 10 (2), 299–303.

Good, R.J. and Mikhail, R.S.: 1981, The contact angle in mercury intrusion porosimetry. Powder Technology 29 (1), 53–62.

Hamm, S.Y., Kim, M.S., Cheong, J.Y., Kim J.Y., Son, M. and Kim, T.W.: 2007, Relationship between hydraulic conductivity and fracture properties estimated from packer tests and borehole data in a fractured granite. Engineering Geology 92 (1-2), 73–87.

Hanák, J., Breiter, K., Rukavičková, L., Sosna, K., Novák, P., Havlová, V., Nováková, L. and Večerník, P.: 2010, Archive Core Sampling. Dílčí zpráva: FR-TI1/367, 67, (in Czech).

Hassan, M.O. and Burdet, R.F.: 1995, Ultrasonic measurements and static load tests in bridge evaluation. NDT&E International 28 (6), 331–337.

Helmuth, K.H., Siitari-Kauppi, M., Klobes, P., Meyer, K. and Goebbels, J.: 1999, Imaging and analyzing rock porosity by autoradiography and Hg-porosimetry/X-ray computertomography - Applications. Physics and Chemistry of the Earth 24 (7), 569–873.

Hommand-Etienne F. and Houpert, R.: 1989, Thermally induced microcracking in granites, characterization and analysis. International Journal of Rock Mechanics and Mining Sciences & Geomechanical Abstracts 26 (2), 125–134.

International Society for Rock Mechanics: 1977, Suggested methods for determining water content, porosity, density, absorption and related properties and swelling and slake-durability index properties. ISRM Suggested Methods, Pergamon Press, 81–84.

International Society for Rock Mechanics: 1978, Suggested methods for determining sound velocity. International Journal of Rock Mechanics and Mining Sciences & Geomechanical Abstracts 15 (2), 53–58.

International Society for Rock Mechanics: 1979, Suggested methods for determining the uniaxial compressive strength and deformability of rock materials. ISRM Suggested Methods, Pergamon Press, 137–140.

Jarchovský, T.: 2006, The nature and genesis of greisen stocks at Krásno, Slavkovský les area – western Bohemia, Czech Republic. Journal of the Czech Geological Society 51 (3-4), 201–216.

Lion, M., Skoczylas, F. and Ledésert, B.: 2005, Effects of heating on the hydraulic and poroelastic properties of bourgogne limestone. International Journal of Rock Mechanics & Mining Sciences 42, 508–520.

Machek, M.: 2011, Relation of pore space geometry, permeability, and microstructure in low-porosity rocks. Ph.D. Thesis, Faculty of Science, Charles University in Prague, 118 pp.

Möri, A., Mazurek, M., Adler, M., Schild, M., Siegesmund, S., Vollbrecht, A., Ota, K., Ando, T., Alexander, W.R., Smith, P.A., Haag, P. and Bühler, CH.: 2003, Grimsel Test Site Investigation Phase IV (1994-1996): The Nagra-JNC in situ study of safety relevant radionuclide retardation in fractured crystalline rock IV: The in situ study of matrix porosity in the vicinity of a water conducting fracture. Nagra Technical Report NTB 00-08, Nagra, Wettingen.

Najser, J., Sosna, K., Nováková, L., Brož, M., Kasíková, J., Michálková, J., Novák, P., Vaněček, M., Záruba, J.: 2011, The relationship between matrix hydraulic conductivity and P-wave and S-wave ultrasound velocities in granites. Proc. GeoProc2011, Perth, Western Australia, 6-9 July 2011. Paper No: GP023.

Nováková, L.: 2008, Main Directions of the Fractures in the Limestone and Granite Quarries along the Sudetic Marginal fault near Vápenná village, NE Bohemian Massif, Czech Republic. Acta Geodyn. Geomater., 5, No. 1 (149), 49-55.

Nováková, L., Brož, M. and Novák, P.: 2010, Comparative study of geophysical parameters and geochemical analysis in undisturbed granites. In Williams et al. (eds.) Geologically Active. 2010 Taylor & Francis Group, London, 2281–2288.

Nováková, L., Sosna, K., Brož, M., Najser, J. and Novák P.: 2011, Geomechanical parametres of the Podlesí granites and its relationship to seismic velocities. Acta Geodyn. Geomater., 8, 3 (163), 353–369.

Onishi, C.T. and Shimizu, I.: 2005, Microcrack networks in granite affected by a fault zone: visualization by confocal laser scanning microscopy. Journal of Structural Geology 27 (12), 2268–2280.

Pácal, Z. and Pavlů, D.: 1979, Final report of the project 4/09-4, 1976-1979; feldspar raw materials-Krásno. Ústřední ústav geologický, Praha, 54 pp., (in Czech).

Pitcher, W.S.: 1997, The Nature and Origin of Granite. Chapman & Hall, London, 408 pp.

Reimer, L.: 1998, Scanning Electron Microscopy Physics of Image Formation and Microanalysis. Springer-Verlag, Berlin Heidelberg, 533 pp.

René, M.: 1998, Development of topaz-bearing granites of the Krudum Massif (Karlovy Vary pluton). Acta Universitatis Carolinae, Geologica 42 (1), 103–109.

Reuschlé, T., Gbaguidi Haore, S. and Darot, M.: 2006, The effect of heating on the microstructural evolution of La Peyratte granite deduced from acoustic velocity measurements. Earth and Planetary Science Letters 243 (3-4), 692–700.

Ritter, H.L. and Drake, L.C.: 1945, Pore-size distribution in porous materials: pressure porosimeter and determination of complete macropore-size distribution. Industrial & Engineering Chemistry Analytical Edition 17 (12), 782–786.

Rukavičková, L., Breiter, K., Holeček, J., Pačes, T., Procházka, J., Hanák, J., Dobeš, P., Havlová, V., Večerník, P. and Hercík, M.: 2009, Annual Report of the Project in 2009. Dílčí zpráva: FR-TI1/367. 132 pp., (in Czech).

Schild, M., Siegesmund, S., Vollbrecht, A. and Mazurek, M.: 2001, Characterization of granite matrix porosity and pore-space geometry by in situ and laboratory methods. Geophysical Journal International 146 (1), 111–125.

Streckeisen, A.: 1974, Classification and nomenclature of plutonic rocks recommendations of the IUGS subcommission on the systematics of Igneous Rocks. Geologische Rundschau 63, 2, 773-776.

Vasconcelos, G., Lourenco, P.B., Alves, C.A.S. and Pamplona J.: 2008, Ultrasonic evaluation of the physical and mechanical properties of granites. Ultrasonics 48 (5), 453–466.

Washburn, E.W.: 1921, The dynamics of capillary flow. Physical Review 17 (3), 273–283.

Zavoral, J.: 1987, Techniques of the laboratory tests in mechanics of soils and rocks. Mechanics of the Soil – Techniques [in Czech]. Ústřední ústav geologický, Praha, 186 pp.

Zinszner, B., Meynier, P., Cabrera, J. and Volant, P.: 2002, Vitesse des ondes ultrasonores, soniques et sismiques dans les argilites du tunnel de Tournemire. Effet de l'anisotropie et de la fracturation naturelle. Oil and Gas Science and Technology – Review 57 (4), 341–353.

Zisman, W.A.: 1933, Comparison of the statically and seismologically determined elastic constants of rocks. Geology 19 (7), 680–686.